

# An Advanced Dual-Carrier-Based Multi-Optimized PWM Strategy of Three-Level Neutral-Point-Clamped Converters for More-Electric-Aircraft Applications

Feng Guo, *Member, IEEE*, Ahmed M. Diab, *Student Member, IEEE*, Seang Shen Yeoh, Tao Yang, *Senior Member, IEEE*, Serhiy Bozhko, *Senior Member, IEEE*, Patrick Wheeler, *Fellow, IEEE*, and Yue Zhao, *Senior Member, IEEE*

**Abstract**—Since three-level neutral-point-clamped (3L-NPC) power generation units bring much competitiveness to the next-generation electric starter/generator (ESG) system for more-electric-aircraft (MEA) applications, the versatile multi-optimized pulse-width-modulation (PWM) becomes a key enabler to this technology. Regarding the mission profile of the state-of-art ESG, the operating points at the cruise feature a high modulation index and low power factor. This means that the neutral-point potential (NPP) fluctuation becomes severe. Besides, if switching states are not configured properly, not only could the lifetime of capacitors be threatened but also irreversible damage to bearing insulation occurs due to the common-mode voltage (CMV), followed by devastating effects on the reliability of other avionic facilities. Given the limitations of the 270VDC unipolar dc-bus structure, deep flux-weakening currents are constantly required for the high speed, resulting in more machine copper losses. To address these issues without any hardware-level efforts, an advanced PWM strategy with dual-carrier-based implementation is proposed in this paper, which achieves boosted dc-link voltage utilization, CMV reduction and balanced NPP at the same time. Simulation results obtained from Simulink/PLECS and experimental results obtained from a 45 kW, 32 krpm ESG prototype system verify the effectiveness and feasibility of the proposed algorithm.

**Index Terms**—Common-mode voltage, dc-link voltage, neutral-point voltage ripple, starter/generator (S/G), three-level.

## I. INTRODUCTION

THE more-electric-aircraft (MEA) concept brings several benefits to the aviation industry due to more expected fuel efficiency, better environmental impact of emissions and less maintenance cost [1]-[3]. Cutting-edge technology of the MEA applications is to replace three-stage would-field synchronous generators with the integrated electric starter/generator (ESG) system [4]. The ESG system serves as the energy interface for

This work was supported by the Clean Sky 2 Joint Undertaking under Grant 807081.

F. Guo was with the Power Electronics, Machines and Control (PEMC) Group, the Department of Electrical and Electronic Engineering, The University of Nottingham, Nottingham NG7 2RD, U.K. He is now with the Power Electronic System Laboratory at Arkansas (PESLA), Department of Electrical Engineering, University of Arkansas, Fayetteville, AR 72701, USA (email: feng.guo@nottingham.ac.uk; fengg@uark.edu)

A. M. Diab is with the Key Laboratory of More Electric Aircraft Technology of Zhejiang Province, University of Nottingham Ningbo China, Ningbo, China (e-mail: ahmed.diab@nottingham.edu.cn)

S. S. Yeoh, T. Yang, S. Bozhko and P. Wheeler are with the Power Electronics, Machines and Control (PEMC) Group, the Department of Electrical and Electronic Engineering, The University of Nottingham, Nottingham NG7 2RD, U.K. (email: seang.yeoh@nottingham.ac.uk; tao.yang@nottingham.ac.uk; serhiy.bozhko@nottingham.ac.uk; pat.wheeler@nottingham.ac.uk)

Y. Zhao is with the Power Electronic System Laboratory at Arkansas (PESLA), Department of Electrical Engineering, University of Arkansas, Fayetteville, AR 72701, USA (email: yuezhao@uark.edu)

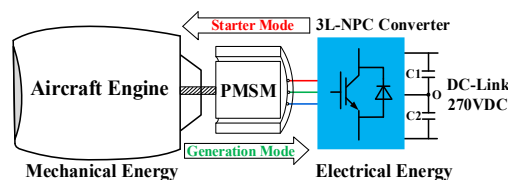


Fig. 1. Configuration of the studied ESG system in the MEA.

delivering electrical power to feed onboard loads. To pursue high power density and high efficiency, the developed system shown in Fig.1 is mainly composed of a high-speed permanent magnet synchronous machine (PMSM) and a power electronics converter. The PMSM is mechanically coupled to the aircraft engine shaft and electrically connected with a bidirectional converter. Compared with the two-level counterpart, the 3L-NPC converter is preferable because of better output harmonics, low voltage stress across switches and reduced  $dv/dt$ , etc.

With respect to other multilevel topologies, extra isolated dc sources are needed for the cascaded H-bridge (CHB) inverters [5], and bulky capacitors are necessary for flying-capacitor (FC) inverters [6]. As the weight and volume of airborne equipment are of importance to the aerospace industry, the classic diode-clamped three-level converter with a single dc source given in Fig.2 is selected as a candidate for design and manufacturing. As for the developed S/G system, the converter works as an inverter in the starter mode, aiming for cranking the aircraft's main engine by motor drives. When the machine speed reaches 10 krpm, the engine ignites at that time. After that, the ESG system is in standby mode. Once the engine speed approaches 20 krpm, the power generation mode activates. In this mode, the engine cranks the PMSM that works as an electric generator, and the 3L-NPC converter operates as a rectifier to convert this ac power to dc for the electric power system (EPS).

It is worth noting that the 3L-NPC converter plays a crucial role in energy flow paths, determining efficiency and reliability. Nevertheless, one of the challenges for such a capacitor bank-split topology is the neutral-point (NP) voltage imbalance problem. Capacitor voltage deviation renders phase voltage distortion on the motor side and the undesirable low-frequency NP potential (NPP) fluctuation puts the lifetime of capacitors at risk. Though large capacitance can alleviate the above demerits, oversize issues induce inevitably. Compared with hardware-intensive solutions to keep NP voltage balanced [7], [8], the advanced modulation strategies are simple but powerful alternatives, which have drawn much attention in recent studies. Among them, the space-vector modulation (SVM) scheme [9] features a degree of freedom for space-vector selection and switching pattern configuration. The carrier-based modulation (CBPWM) [10] offers a chance to simplify the modulation

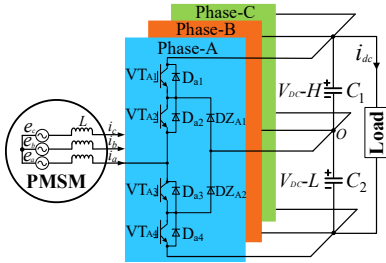


Fig. 2. Topology of the 3L-NPC converter.

process by injecting appropriate zero-sequence voltage (ZSV). However, the high modulation index (MI) and low power factor (PF), as the steady-state characteristics of the ESG system, aggravate the NP voltage oscillation and deviation. To solve this drawback for all loads, the nearest-three-virtual-space-vector (NTV<sup>2</sup>) modulation scheme is proposed in [11]. In the works of [12], with generalized bias-offset injection, a novel active NPP balancing control algorithm is studied for the supplement of the NTV<sup>2</sup> strategy. In [13], the model-predictive-control (MPC) based NTV<sup>2</sup> method is explored to improve the dynamic response of T-type three-level inverters.

Due to the higher common-mode voltage (CMV) produced by the original virtual-space-vector (VSV), premature damage to winding insulation has an adverse effect on the reliability of a machine, especially for the studied aerospace drives. Hence, those switching states resulting in high components of CMV need to be substituted. In [14], with the hysteresis control and logic blocks, a modified NTV<sup>2</sup> scheme is proposed to reduce switching losses and CMVs. The authors in [15] use small and medium vectors to synthesize new virtual small vectors that participate in the reference voltage vector approximation. This facilitates capacitor voltage balance and CMV suppression at the same time. As the medium vectors are characterized by zero CMV and their NP currents alternate three-phase currents over a line cycle, an enhanced NTV<sup>2</sup> strategy is presented in [16]. However, the pulse train of the aforesaid approaches features multi-segments and the opposite dc-rail clamping sequence. More importantly, SVM-based implementations cause a heavy computation burden when using fast-switching devices.

Furthermore, based on the standard of MIL-STD-704F [17], the rated voltage of the aircraft's main dc-bus is 270VDC though 250~280VDC operation is allowed by the droop control [18]. It indicates that the back electromotive force (EMF) of the motor is large when operating in the generation mode. For the sake of a higher shaft speed under limited converter/machine output capability, the deep flux-weakening (FW) current is constantly required, thereby leading to more machine copper losses. To overcome this disadvantage, in contrast with the latest conceptualization of medium-voltage EPS [19], a boosted dc-link voltage utilization would be a straightforward solution that avoids partial discharge issues and superconducting barriers. In the existing literature, the third-order harmonic voltage injection (THVI) method was broadly considered. For the active split dc-bus four-leg inverter [20], the THVI is effective for controlling the fourth leg independently as well as a higher utilization on the dc-link voltage. With respect to the two-stage matrix converter [21], a ZSV is added to the phase leg reference voltages to improve dc-link voltage utilization. In

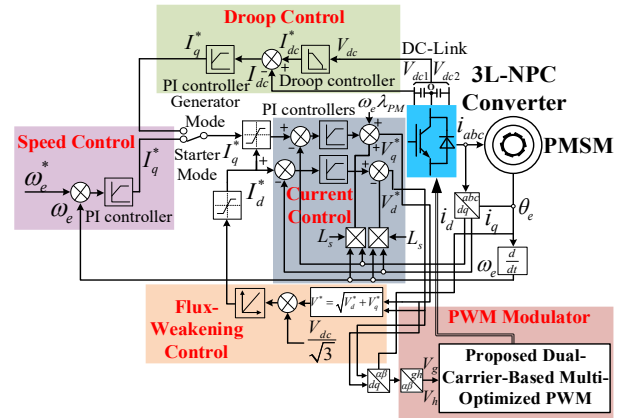


Fig. 3. Control blocks of the developed ESG system.

multiphase induction motor (IM) drives [22], a third harmonic is also injected for torque-enhancement purposes. As for the modular multilevel converter (MMC) [23], not only can THVI boost dc-link voltage utilization but also mitigate capacitor voltage ripple and circulating current. However, all the above algorithms only focus on the linear modulation improvement, which is still quite limited. In other words, the operating points of the converter are further required to be extended into the overmodulation region. For two-level topology, in accordance with the reference voltage vector track, a continuous PWM algorithm has been studied in [24]. The method consists of two modes until it transits to the six-step operation. An approach in [25] defines a holding angle and a reference space vector angle. Thus, the desired MI can be precisely manipulated by the Fourier series expansion. In [26], an overmodulation scheme with the phase current reconstruction is reported for PMSM drives. An optimized PWM strategy is proposed in [27] for the minimum harmonic distortion in overmodulation conditions, particularly for inverter-fed high-speed drives with a low-carrier ratio. To satisfy the overmodulation conditions for the 3L-NPC topology, a CBPWM has been studied for IM drives with dynamic loads [28], which extends the operating point into the overmodulation region. It is noticeable that the ZSV affects the performance of the NPP balance. Aiming to obtain perfect capacitor voltage balance regardless of output voltages and PFs, [29] and [30] give two polygon compression technologies for the original NTV<sup>2</sup> strategy, but the implementation highly relies on the dwell-time calculation in every PWM sampling time.

In this paper, an advanced dual-carrier-based PWM strategy is proposed for the ESG system in MEA applications. An initial attempt at an enhanced modulation strategy is studied in [31], wherein a reference voltage vector trajectory, by the sextant-coordinate system, is incorporated with the CMV-reduced pulse train. However, the method is unfavorable for implementation in digital controllers. In this paper, a novel dual-carrier-based modulation technique is proposed with advanced pulse train generation, detailed algorithm verification, output performance comparison, and discussion. The proposed PWM realizes multi-objective optimization at once, that is, NPP ripple elimination, CMV suppression, and boosted dc bus voltage utilization. To improve computational efficiency, dedicated modulation signals are analytically derived by exploiting the coordinates of the programmed reference voltage vector's track.

TABLE I  
 THE SWITCHING PRINCIPLES OF 3L-NPC CONVERTER

Switching State	SWITCH STATUS				Output Voltage Level
	VT <sub>x1</sub>	VT <sub>x2</sub>	VT <sub>x3</sub>	VT <sub>x4</sub>	
[P]	1	1	0	0	$V_{dc}/2$
[O]	0	1	1	0	0
[N]	0	0	1	1	$-V_{dc}/2$

Compared with the works of [31], the major contributions and supplemental validations of this study are given as follows:

- 1) Dual-carrier waves are employed to implement inverse pulse trains with balanced NPP and reduced CMV magnitude.
- 2) Three-phase modulation signals are defined by algebraic coordinates of the reference voltage vector in the first sextant.
- 3) The information of the polygonal track of vector vertex coordinate is merged into modulation waves.
- 4) Losses breakdown of the 3L-NPC converter and PMSM are presented with the addition of analysis and comparison.
- 5) The trajectory of operating points of the ESG system with the proposed PWM algorithm is discussed, together with the resultant  $dq$ -axis currents and the output torque capability.
- 6) Extensive simulation and experimentation are carried out to verify the effectiveness of the proposed PWM technique.

The rest of the paper is organized as follows. Section II gives the principle of the ESG system. Section III reviews a CMV-reduced NTV<sup>2</sup> solution. The proposed PWM algorithm is studied in Section IV, including the operational analysis under overmodulation conditions. The simulation and experimental results are presented in Sections V and VI, respectively. Finally, Section VII draws the main conclusions of this work.

## II. PRINCIPLES OF ESG SYSTEM

### A. Control Design of ESG System

For the designed aircraft ESG system, the surface-mounted PMSM is chosen due to its high-power density, high torque-to-current ratio, and fault tolerance capability. Although high efficiency can be sometimes obtained by increasing pole-pair numbers, the low pulse-ratio problem comes with high-speed operation. Considering these factors, a 6-pole 36-slot machine is selected as a candidate for the target systems [4].

Fig.3 displays the overall control blocks. As shown, the outer control loop consists of the FW control, aiming to operate in high-speed regions, the motor speed control for the startup process, and the dc-link current is controlled based on the droop characteristics. The inner control loop is designed for current control. The magnitude of the space vector is still calculated by the classic current PI control because of its robustness. The vector control technique is adopted for machine decoupling purposes and linearizing its mathematical model. It implies that the flux and torque can be controlled independently. Hence, machine torque represented as active power can be controlled by  $q$ -axis current. Noteworthy, in power generating mode, a large negative  $d$ -axis current must be constantly injected to handle the large back EMF, which causes a lower PF angle.

### B. PMSM Model and Operating Constraints

The  $dq$ -axis models of the PMSM are given as follows:

$$T_{em} = \frac{3}{2} n_p \cdot [\varphi_f \cdot i_q + (L_d - L_q) \cdot i_d \cdot i_q] \quad (1)$$

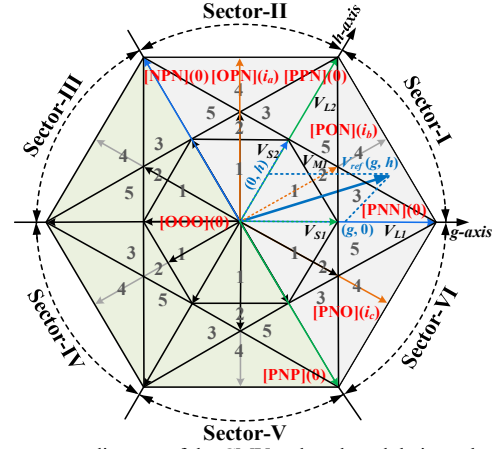


Fig. 4. Space vector diagram of the CMV-reduced modulation scheme.

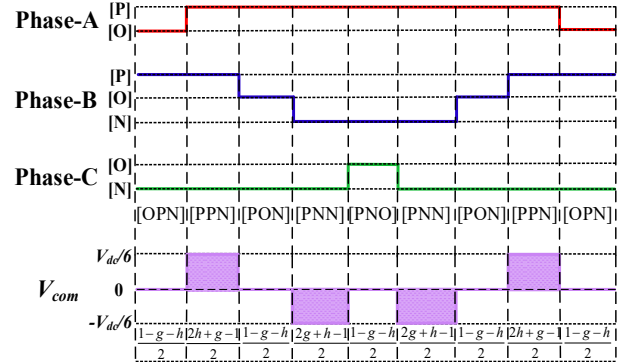


Fig. 5. Pulse trains and associated CMVs for subsector-4 of Sector-I.

$$V_d = R \cdot i_d + L_d \frac{di_d}{dt} - \omega_e \cdot L_q \cdot i_q \quad (2)$$

$$V_q = R \cdot i_q + L_q \frac{di_q}{dt} + \omega_e \cdot L_d \cdot i_d + \omega_e \cdot \varphi_f \quad (3)$$

where  $T_{em}$  is the electromagnetic torque,  $n_p$  refers to the pole-pair numbers,  $\varphi_f$  is the permanent magnet flux linkage,  $V_d$ ,  $V_q$  and  $i_d$ ,  $i_q$  represent the  $dq$ -axis components of motor voltage and current,  $L_d$  and  $L_q$  are the  $dq$ -axis inductances,  $\omega_e$  is the electrical angular frequency and  $R$  is the stator winding resistance.

For the applied PMSM,  $dq$ -axis inductance shares the same value. This implies that the electromagnetic torque of the machine is only provided by permanent magnet torque, which is the first term in (1). As the maximum machine stator voltage, denoted by  $V_{lim}$ , is determined by the dc-link voltage and PWM strategy, the corresponding limitation can be written as:

$$\left(i_d + \frac{\varphi_f}{L_d}\right)^2 + i_q^2 = \left(\frac{V_{lim}}{\omega_e L_q}\right)^2 \quad (4)$$

Considering the capacity of the designed machine/converter, the maximum current value denoted by  $I_{max}$ , should fulfill:

$$i_d^2 + i_q^2 \leq I_{max}^2 \quad (5)$$

The solution of (4) and (5) determines an overlapped area of voltage and current limit circles, which restricts the allowable operating zones of the studied ESG system.

### C. Three-Level NPC Converter

Fig.2 shows the circuit diagram of the 3L-NPC converter that consists of four IGBTs ( $VT_{x1} \sim VT_{x4}$ ) and two clamping diodes ( $DZ_{x1}$  and  $DZ_{x2}$ ), where  $x = \{A, B, C\}$ . Two equal capacitors ( $C_1$  and  $C_2$ ) are series-connected to form the EPS. This topology clamps the pole voltage to the midpoint, positive and negative

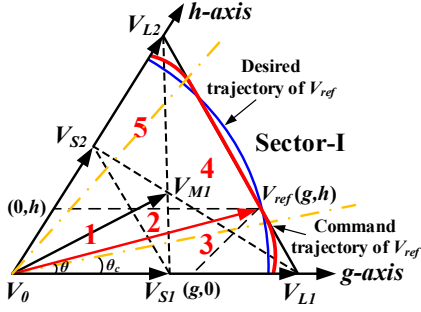


Fig. 6. The VSV-based PWM strategy for operating at the OM-I in Sector-I.

rail of the dc-bus. Therefore, three-level output voltages ( $\pm V_{dc}/2$  and 0) are produced. Table I details the relationship among the switching state, switch status, and output voltage level.

### III. REVIEW OF ENHANCED VIRTUAL-SPACE-VECTOR MODULATION STRATEGY

#### A. The G-H Reference Frame

With a transformation matrix in (6), duty cycles can be calculated by algebraic functions, as opposed to complex trigonometric functions in the orthogonal reference frame [12].

$$\begin{bmatrix} V_g \\ V_h \end{bmatrix} = \begin{bmatrix} 1 & -1/\sqrt{3} \\ 0 & 2/\sqrt{3} \end{bmatrix} \begin{bmatrix} V_\alpha \\ V_\beta \end{bmatrix} \quad (6)$$

By using the volts-second rule in the 60-degree plane,  $V_g$  and  $V_h$  can be therefore calculated as:

$$\begin{cases} V_g = X_g d_1 + Y_g d_2 + Z_g d_3 \\ V_h = X_h d_1 + Y_h d_2 + Z_h d_3 \end{cases} \quad (7)$$

where  $(V_g, V_h)$ ,  $(X_g, X_h)$ ,  $(Y_g, Y_h)$  and  $(Z_g, Z_h)$  represent the position of space vectors in the  $g$ - $h$  reference frame.  $d_1$ ,  $d_2$  and  $d_3$  denote the duty cycles of the nearest-three space vectors.

#### B. The Definition of CMV-Reduced Virtual Space Vectors and Their Associated Pulse Trains

The CMV is defined as the voltage between the midpoint of the AC-side and the NP of the dc-link, which is calculated by:

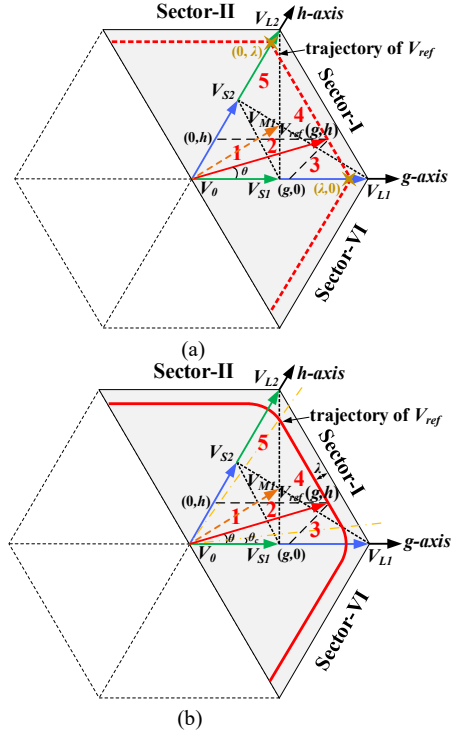
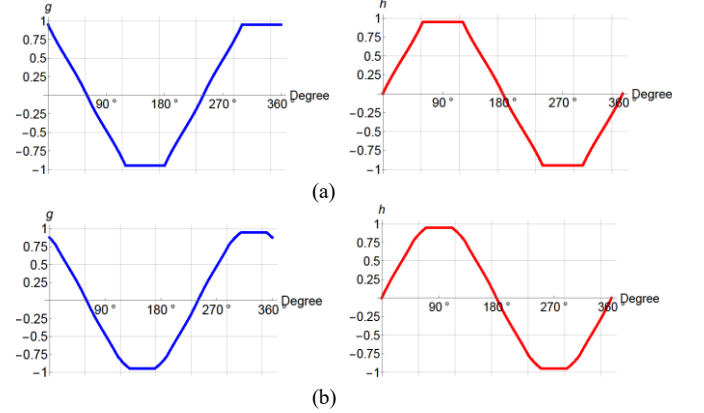
$$V_{com} = \frac{1}{3}(V_{ao} + V_{bo} + V_{co}) \quad (8)$$

where  $V_{ao}$ ,  $V_{bo}$  and  $V_{co}$  refer to three-phase pole voltages.

According to the series of reformulated VSVs presented in [16], two pairs of large vectors are exploited to compose two virtual small vectors, and adjacent three medium vectors synthesize a virtual medium vector, whereas the selection of zero and large vectors follow the same rule of the original NTV<sup>2</sup> scheme. As shown in Fig.4, the blue, orange, and green dashed arrow lines represent these modified VSVs defined as follows:

$$\begin{cases} V_{S1} = [V_{[PPN]}(0) + V_{[PNP]}(0)]/2 \\ V_{S2} = [V_{[PNN]}(0) + V_{[NPN]}(0)]/2 \\ V_{M1} = [V_{[OPN]}(i_a) + V_{[PON]}(i_b) + V_{[PNO]}(i_c)]/3 \\ V_0 = V_{[OOO]}(0) \\ V_{L1} = V_{[PNN]}(0) \\ V_{L2} = V_{[PPN]}(0) \end{cases} \quad (9)$$

where the subscript bracket of the space vector indicates the selected switching state and the value in the parentheses refers to the corresponding NP current.


 Fig. 7. Reference voltage vector trajectory with a compression factor  $\lambda$  by (a) Hexagonal boundary limit. (b) Circular + hexagonal locus.

 Fig. 8. The  $g$ - $h$  coordinate of the reference voltage vector in the case of  $\lambda=0.97$  with (a) Hexagonal boundary limit. (b) Circular + hexagonal trajectory.

And then, the dedicated switching sequence can be arranged, accordingly. On the one hand, the corresponding switching states in (9) can determine the CMVs through (8), resulting in one-sixth of the dc-link voltage. On the other hand, the value in the bracket of equation (9) represents the NP current produced by the adopted space vector. Therefore, the average null NP current is always fulfilled. Based on the above elucidation, it concludes that not only can the enhanced NTV<sup>2</sup> scheme obtain balanced NPP for all loads but also the CMV magnitude is suppressed. Fig.5 shows the pulse trains and associated CMVs by this dedicated PWM approach in subsector 4 of Sector-I. Additionally, it can be observed that, with the help of the  $g$ - $h$  reference frame, the duty cycle of each switching state has been expressed by coordinate-based algebraic operations.

### IV. PROPOSED ADVANCED DUAL-CARRIER-BASED MULTI-OPTIMIZED PWM TECHNIQUE

In this paper, the MI, denoted as  $m$  in (10), is defined as the

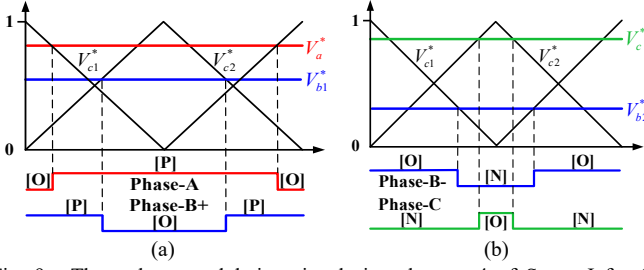


Fig. 9. Three-phase modulation signals in subsector-4 of Sector-I for (a) Positive pulse train generation (b) Negative pulse train generation.

ratio between the magnitude of the desired reference voltage vector and the radius of the inscribed circle of the hexagon.

$$m = \frac{|V_{ref}|}{V_{dc} / \sqrt{3}} \quad (10)$$

Based on the value of (10), the operating regions of the 3L-NPC converter can form three groups, i.e., linear modulation (LM), overmodulation mode-I (OM-I), and overmodulation mode-II (OM-II). If the reference voltage vector traces a circular trajectory inside the hexagon, it obtains the LM. This means that the MI ( $0 < m \leq 1$ ) arises along with the length of the output vector until the trajectory is inscribed on the hexagon side. As for the OM-I mode, the radius of desired reference voltage vector is between the inscribed circle and circumscribed circle of the hexagon. This indicates a higher MI ( $1 < m \leq 1.05$ ). In this scenario, the tip of the output vector transits from a circular trajectory and then moves along the hexagon side once its vertex exceeds the boundary of the hexagon. As can be seen from Fig.6, a crossover angle ( $\theta_c$ ) maintaining the trajectory inside half of the sextant can be regulated so that extending the fundamental component of output voltage. To be more exact, the reference voltage vector is fixed by a holding angle ( $\theta_h$ ) for a period before jumping to the straight line of the hexagon. In case  $\theta_h$  equals  $30^\circ$ , the classic six-step mode yields, which constrains the MI of 1.1 for the OM-II mode [24].

Since the output performance of a converter degrades along with a deepening MI [25], the ac variables of the OM-II mode are not suitable for high-speed drives in aerospace applications. As a result, the scope of this work primarily focuses on the operation under OM-I mode, thereby extending the output voltage of the studied 3L-NPC converter. The preset reference voltage vector's locus is incorporated with the aspects of NPP balance, CMV reduction and simplified modulation process. More detailed explanations are given in the following texts.

#### A. The Programmed Trajectory of Reference Voltage Vector with Sextant coordinate

Based on the above principle of overmodulation operation and the geometry relationship plotted in Fig.6, the sextant coordinate ( $g, h$ ) of the hexagon side can be derived in (11). It is noted that the length of  $V_{ref}$  is normalized with the magnitude of  $V_{Ll}$ . Thus,  $g$  and  $h$  conveniently point to the position of  $V_{ref}$ .

$$\begin{cases} \frac{|V_{ref}|}{\sin 60^\circ} = \frac{1}{\sin(120^\circ - \theta)} \\ \frac{|V_{ref}|}{\sin 120^\circ} = \frac{h}{\sin \theta} = \frac{g}{\sin(60^\circ - \theta)} \end{cases} \quad (11)$$

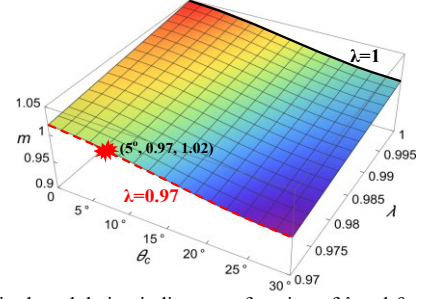


Fig. 10. Desired modulation indices as a function of  $\lambda$  and  $\theta_c$ .

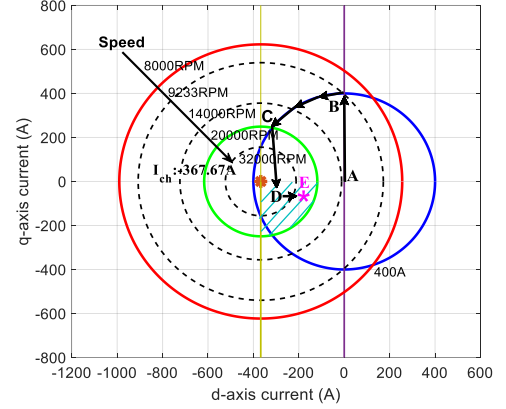


Fig. 11. Operating trajectory of the studied ESG system.

The solution of the above equation is calculated as:

$$\begin{cases} g = \frac{\sin(60^\circ - \theta)}{\sin(120^\circ - \theta)} \\ h = \frac{\sin \theta}{\sin(120^\circ - \theta)} \end{cases} \quad (12)$$

where  $\theta$  is the rotating angle of the reference voltage vector.

For the conventional NTV<sup>2</sup> strategy, the hexagon boundary limit with a compression factor ( $\lambda$ ) for  $n$ -level NPC converters [11] was explored, aiming to extend the LM into the OM region. Inspired by this algorithm, multiplying (12) by  $\lambda$  can therefore specify  $V_{ref}$  that tracks the dashed red hexagon plotted in Fig.7(a). Moreover, by adapting  $\theta_c$ , a circular trajectory is added to the locus in order to trade dc-link voltage utilization against output harmonics, as shown in Fig.7(b). In the case of  $\lambda=0.97$ , the associated  $g$ - $h$  coordinates for these two occasions are presented in Fig.8. In conclusion, with the help of the enhanced coordinate-based pulse trains presented in Fig.5, the operational region of the presented ESG system with 270VDC is enabled to be enlarged, together with balanced NPP and suppressed CMV.

#### B. Dual-Carrier-Based Modulation Technique for Hexagon-Compression Technique

It can be seen from Fig.5 that the switching patterns for the CMV-reduced NTV<sup>2</sup> scheme feature 9-segment. It indicates that the conventional SVM implementation would take up extra computational resources because of the complicated dwell-time determination and switching pattern configuration.

Without loss of generality, herein, subsector-4 of the first sector is taken as an example to present the dual-carrier-based implementation for streamlining the proposed PWM. Since the clamping sequence for phase-B is carried out as [P]→[O]→[N], as opposed to phase-A and C. To generate such a pulse train, two decomposed modulation signals are required, denoted as

TABLE II  
 ESG SYSTEM PARAMETERS

Parameters	Value
$L_d = L_q$	99 $\mu\text{H}$
Pole-pair numbers	3
Switching frequency	16 kHz
PM flux	0.03644 $\text{Vs/rad}$
Base speed	8000 rpm
Fundamental frequency in generation mode	1~1.6 kHz
Capacitor Value ( $C_1=C_2$ )	600 $\mu\text{F}$
DC-link Voltage	270 V

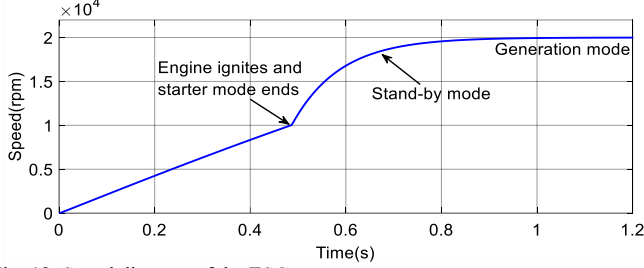
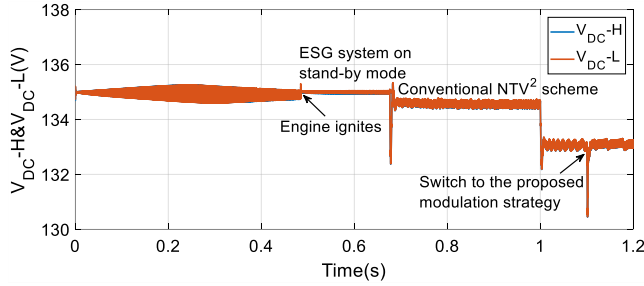


Fig. 12. Speed diagram of the ESG system.


 Fig. 13. Capacitor voltages of the ESG system with the conventional NTV<sup>2</sup> scheme and the proposed modulation strategy.

$V_{b1}^*$  for Phase-B+ and  $V_{b2}^*$  for Phase-B-, together with two reversely ordered carrier waves, represented as  $V_{c1}^*$  and  $V_{c2}^*$ .

In accordance with similar triangles displayed in Fig.9, the modulation signals can be yielded as follows:

$$\begin{cases} V_a^* = g + h \\ V_{b1}^* = h \end{cases}; \begin{cases} V_{b2}^* = g \\ V_{c1}^* = g + h \end{cases} \quad (13)$$

As for positive pulse train generation, i.e., [P]→[O],  $V_a^*$  and  $V_{b1}^*$  are compared with  $V_{c1}^*$  and  $V_{c2}^*$ , respectively. The TRUE value refers to [P] while the FALSE manifests [O]. With respect to negative pulse train generation, i.e., [O]→[N], the TRUE value represents [N] while the FALSE value indicates [O].

It is known from (13) that the three-phase modulation waves are the functions of sextant coordinates. Then, with the preset loci displayed in Fig.8, the overmodulation condition for the used 3L-NPC converter can be easily fulfilled.

### C. Analysis of DC-Link Voltage Utilization Ratio and The Operational Changes of ESG System

In terms of the trajectory shown in Fig.7(b), its fundamental component can be calculated by the Fourier series expansion:

$$F(\theta) = \frac{\pi}{4} \int_0^{\pi/2} |V_{ref}(\theta)| \cdot \sin \theta \cdot d\theta \quad (14)$$

Fig.10 presents the 3D plot of the desired modulation indices as a function of  $\theta_c$  and  $\lambda$  that ranges from 0.97 to 1, in which the unity compression factor leads to the maximum dc-link voltage utilization. Hence, the converter's output capability constrained

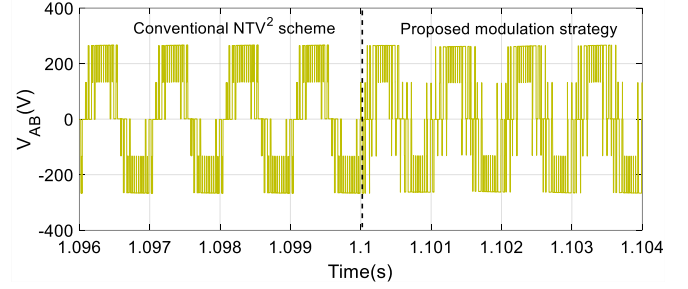
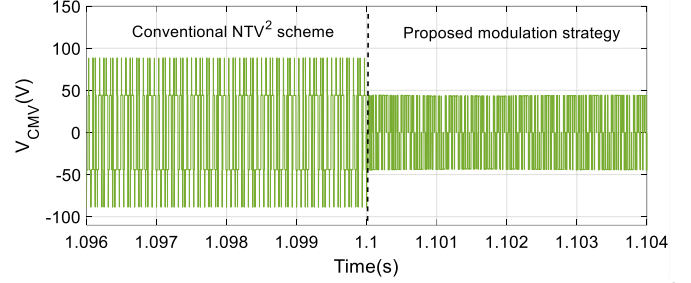
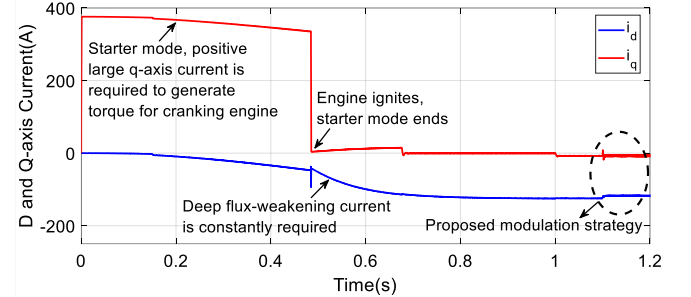


Fig. 14. Line-to-line voltage during the PWM method transition instant.


 Fig. 15. CMV comparison of the ESG system with the conventional NTV<sup>2</sup> scheme and the proposed modulation strategy.

 Fig. 16. Simulated  $dq$ -axis currents of the ESG system during the entire-speed range operation.

by a definite dc-link voltage of 270VDC would be expected to improve in the generation mode, together with a lower FW current. For example, the MI is around 1.02 when  $\theta_c$  and  $\lambda$  are set at  $5^\circ$  and 0.97, respectively. Moreover, the black curve in Fig.10 refers to the reachable MI when the reference voltage vector tracks the outline of the hexagon. While the MI is a bit higher than its counterpart with a red dotted line, more deterioration would be expected on the AC side.

Fig.11 displays the operating trajectory of the studied ESG system. As shown, in the starter mode, point A moves along the maximum torque per amp (MTPA) line until point B at the base speed of the motor drives, i.e., 9233 rpm. With the machine speed ramping up further, the operating point passes through point C, followed by point D in the power generating region. At last, it approaches point E, along with the reduced  $d$ -axis current, if a higher dc-link voltage utilization is reached.

## V. SIMULATION RESULTS

The simulated model of the aircraft ESG system illustrated in Fig.3 is built in the Simulink/PLECS environment, and the parameters can be found in Table II.

### A. Capacitor Voltage Balance Over Wide-Range Operation

In the simulation setup, the system initially runs in the starter mode, and then the FW control activates at 0.45s. After that, the aircraft's main engine ignites. The power-generating mode

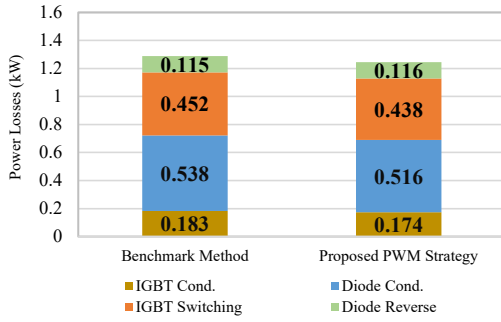


Fig. 17. Power losses breakdown between the benchmark method and the proposed PWM strategy in the power generation mode.

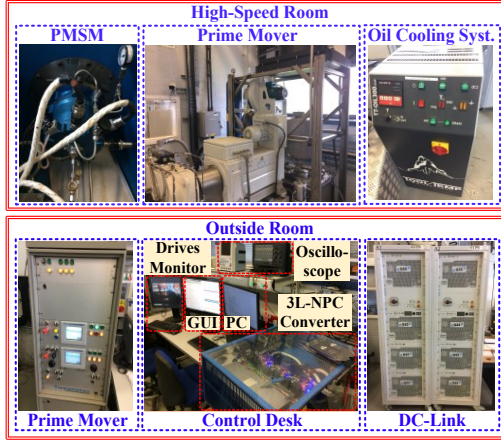


Fig. 18. Experimental test rig.

starts by connecting a 3 kW resistive load to the dc-link at 1s with a machine speed of 20 krpm, and the voltage droop control takes over dc-link voltage regulation at the same time. At 1.1s, the gating pulses transit from the conventional NTV<sup>2</sup> strategy chosen as the benchmark method in the following tests to the proposed PWM, in which the compression factor  $\lambda$  is 0.98 and the crossover angle  $\theta_c$  is 12.5°. The average MI and PF are 0.95 and 0.15, respectively. The speed diagram of the ESG system is described in Fig.12. In Fig.13, the simulation results show that upper and lower-side capacitor voltages ( $V_{DC-H}$  and  $V_{DC-L}$ ) maintain the same value over the wide-speed operation. Furthermore, the line-to-line voltage by the presented PWM scheme is shown in Fig.14. As shown, the output voltages of this converter feature five levels over a fundamental period, which thus exhibits the characteristics of three-level converters.

### B. Common-Mode Voltage Reduction

The CMVs generated by the benchmark method and the proposed modulation strategy are shown in Fig.15, respectively. It can be observed that, compared with the NTV<sup>2</sup> scheme, the amplitude of the presented method has been reduced to half.

### C. Improvement of DC-Link Voltage Utilization

Fig.16 shows the simulated  $dq$ -axis currents of the studied ESG system. After switching to the proposed PWM algorithm at 1.1s, the  $d$ -axis current roughly reduces from -125A to -117A. This represents that the large FW depth has been relieved due to the boosted dc-link voltage utilization. It is worth noting that the  $q$ -axis current ripple is inevitably increased because of the non-circular locus of the reference voltage vector.

### D. Power Losses Analysis

The power losses are calculated by the thermal model of the

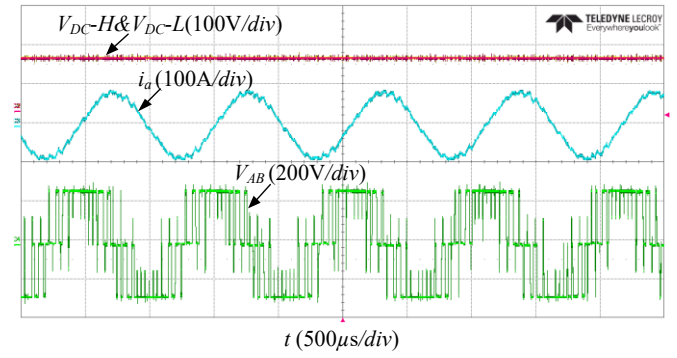


Fig. 19. Experimental results of the proposed modulation scheme ( $\lambda=0.98$  and  $\theta_c=12.5^\circ$ ) during the steady state.

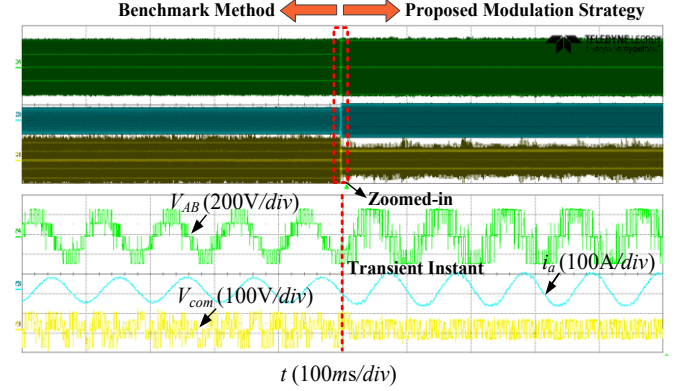


Fig. 20. Experimental results of the proposed modulation scheme ( $\lambda=0.98$  and  $\theta_c=12.5^\circ$ ) during the dynamic state.

applied Infineon F3L400R07ME4\_B22/B23 insulated-gate bipolar transistor (IGBT) power module that has a maximum collector-emitter voltage of 650V and continuous collector current of 400A. According to the manufacturer's datasheet, the losses can be obtained through the PLECS tools. The switching frequency is set at 16 kHz. Before transiting to the proposed modulation strategy, the MI is 0.95. With 25 kW of active power generation at a speed of 20 krpm, the semiconductor losses breakdown is shown in Fig.17. It can be seen that the presented PWM technique achieves lower conduction losses on both IGBTs and diodes. This is because, when the ESG system delivers the same active power, the required FW current no longer needs to be kept at such a higher value that handles the large machine's back EMF.

Moreover, by importing the data of phase currents into the finite element analysis (FEA) model of the used PMSM, its copper loss can be calculated when the fundamental frequency of the target system runs at 1 kHz. The results show that the value is significantly reduced from 152.63 W to 135.29 W.

### E. Comparison with Other Modulation Strategies for 3L-NPC Converter-Fed Electric Motor Drive Applications

In contrast with the recent modulation schemes for 3L-NPC converter-fed motor drives in the literature, the proposed PWM technique achieves the following advantages:

1) Since the trajectory of the reference voltage vector is regulated based on dedicated pulse trains, the operational region of the target drives is enlarged, together with other benefits, such as inherent NP voltage balance, NPP ripple elimination and suppressed CMVs. However, references [12], [14], [32]-[37] cannot realize such multi-objective optimization.

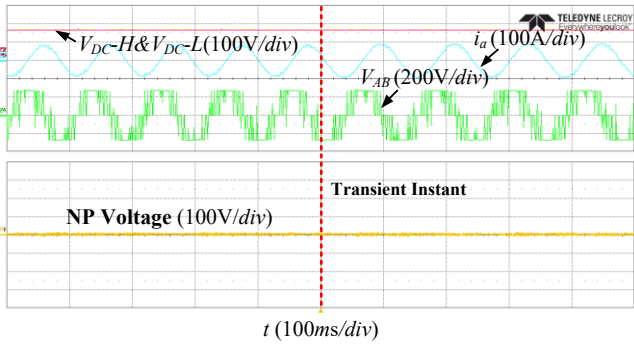


Fig. 21. Experimental results of the proposed modulation scheme ( $\lambda=0.98$  and  $\theta_c=5^\circ$ ) during the dynamic state.

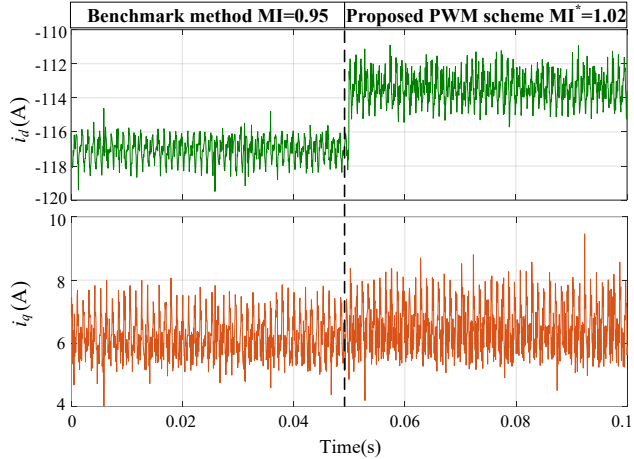


Fig. 22. Experimental results of the  $dq$ -axis currents.

2) The VSVs are exploited in this work to achieve minimized NP voltage fluctuation, but the prior modulation strategies in [32], [34] and [35] for three-phase PMSM drives fail to address this issue properly. Similarly, for a multi-phase IM drive in [37], not only can a VSV-based direct torque control (DTC) method ensure balanced NP voltage but also brings a good dynamic response of speed and torque over a wide speed range operation.

3) This approach does not compromise on CMV magnitude in specific operating points, i.e.,  $\pm 1/6V_{dc}$  over the entire speed range operation. Nevertheless, most of the CMV-reduced PWM derived in [36] is only suitable for low speed.

4) By implementing coordinate-based modulation signals, the presented dual-carrier-based PWM scheme notably reduces complexity compared with the works of [14] and [32]-[34].

Noteworthy, the turn-on/off operations over a switching cycle by the proposed algorithm is more than the other methods in [14] and [32]-[36]. It implies that the advantages are obtained at the expense of extra switching loss. By contrast, due to non-switching intervals in some carrier periods, the studies in [35] and [36] are helpful for lower power losses on semiconductors.

## VI. EXPERIMENTAL RESULTS

The modulation performance of the proposed dual-carrier-based multi-optimized PWM technique is verified by a 45 kW, 32 krpm laboratory-built aircraft ESG prototype system. The experimental test rig is illustrated in Fig.18. A 150 kW prime mover and a high-speed machine are placed in an isolated room for safety considerations. The prime mover mechanically emulates an aircraft engine shaft that is coupled to the high-

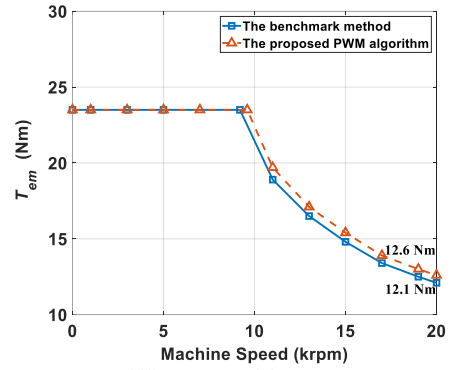


Fig. 23. Output torque capability curves of the ESG system.

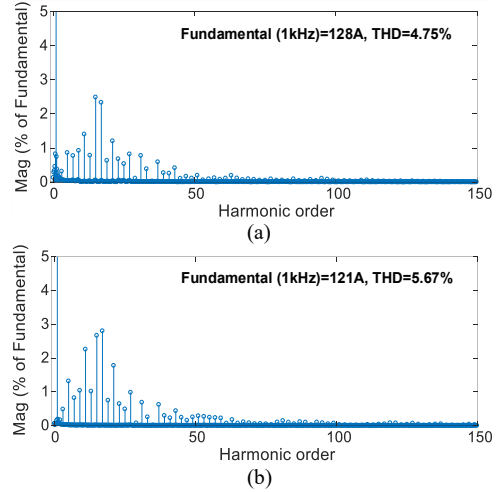


Fig. 24. Harmonic spectra of phase current under the steady-state operating point with (a) The benchmark method. (b) The proposed PWM algorithm.

speed PMSM. TMS320C6713 DSP Starter Kit (DSK) and an Actel FPGA-ProASIC A3P400 card are selected as the control platform. AC-side parameters are monitored by the PPA5530 power analyzer. Since phase currents direction changes rapidly at light-load conditions, which aggravates the capacitor voltage imbalance, the experimentations primarily focus on a light-load condition under the power generating mode of the ESG system, whereas the starter mode is not presented here as it takes up a short time compared with the whole period.

### A. Steady-State Performance

Fig.19 shows the experimental results of capacitor voltage, phase current and line-to-line voltage when the proposed PWM approach with  $\lambda=0.98$  and  $\theta_c=12.5^\circ$  performs at a MI of 0.95 and a PF of 0.15. As can be seen, the voltages across the two capacitors are maintained at a balanced state.

### B. Dynamic-State Performance

Fig.20 gives a transient instant when the firing pulses switch from the benchmark method to the proposed advanced PWM algorithm under a step change in load current. This scenario represents that the aircraft ESG system requires a higher output capability and meets more active power demand simultaneously. As shown, the magnitude of CMV generated by the proposed modulation strategy reduces to half of that of the counterpart. Moreover, a smooth transition in phase current can be observed. In Fig.21, the experimentations regarding the NPP, line-to-line voltage and phase current are obtained during a step-change in machine speed if  $\lambda$  is set at 0.98 and  $\theta_c$  is  $5^\circ$ . This condition corresponds to the fundamental frequency decreasing from 1

kHz to 850 Hz. The above results demonstrate a good dynamic-state performance of the proposed PWM technique.

### C. DQ-Axis Currents and Output Torque Performance

To assess the proposed PWM strategy on  $dq$ -axis currents and output torque, here,  $\lambda$  and  $\theta_c$  are chosen as 0.97 and  $\theta_c=10^\circ$ , respectively. The direct and quadrature axis currents obtained from the Graphic User Interface (GUI) are shown in Fig.22. As can be seen, the  $d$ -axis current roughly reduces from -117 A to -113 A when the presented modulation algorithm gets involved. Through the FFT analysis of the 3L-NPC converter's output voltage under this situation, the result confirms a MI of 1.02, which is the reason for the phenomenon of FW current reduction. Furthermore, the  $dq$ -axis current ripple has increased. Under the aforesaid operating conditions, the output torque capability curves of the target drive systems are shown in Fig.23. It can be observed that the maximum electromagnetic torque by the provided PWM algorithm is approximately 12.6 Nm, raised by 4.13% in contrast with the benchmark method.

### D. Distortion Analysis

The total harmonic distortion (THD) analysis of the output phase current is conducted when the PWM modulator changes its switching patterns. Compared with the benchmark method of 4.75%, the THD of the proposed PWM is 5.67%. A possible reason for this consequence is that the reference voltage vector is not approximated by the nearest three space vectors, and it tracks a non-circular trajectory over a fundamental period.

### E. Computational Time

To evaluate the algorithmic efficiency of the proposed PWM, the execution time was tested on the digital controller kit. The results show that this dual-carrier-based multi-optimized PWM method costs about 48.6 $\mu$ s in contrast with the computational time of 65.3 $\mu$ s using the conventional SVM implementation, which presents the low complexity of this work.

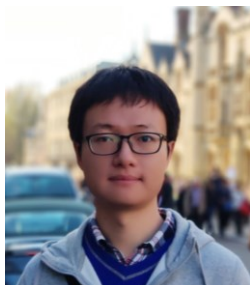
## VII. CONCLUSION

In this paper, a novel dual-carrier-based modulation strategy has been proposed for 3L-NPC converters used in aircraft ESG systems. The introduced PWM technique aims to eliminate NP potential oscillation, suppress CMV magnitude and boost dc-link voltage utilization at the same time. Its advancements lie in the following: 1) The simplicity of inversely arranged switching patterns and multi-segment pulse trains that aim to lower the CMV is gained by implementing coordinate-based modulation signals against dual carriers. 2) This method brings an extra degree of freedom for tracking a programmed reference voltage vector's trajectory over a fundamental period. 3) With the help of a MI supplement, large FW currents caused by the MEA unipolar DC-bus structure have been alleviated, together with an improved output capability of motor drive systems and reduced copper loss on the machine. The proposed modulation technique is applicable to other three-level converter-fed motor drives. Simulation and experimental results finally proved the effectiveness and feasibility of the presented PWM strategy.

## REFERENCES

- [1] B. Sarlioglu and C. T. Morris, "More electric aircraft: review, challenges, and opportunities for commercial transport aircraft," *IEEE Trans. Transport. Electrification.*, vol. 1, no. 1, pp. 54-64, Jun. 2015.
- [2] P. Wheeler, T. S. Sirimanna, S. Bozhko and K. S. Haran, "Electric/hybrid-electric aircraft propulsion systems," *Proc. IEEE*, vol. 109, no. 6, pp. 1115-1127, Jun. 2021.
- [3] G. Buticchi, P. Wheeler and D. Boroyevich, "The more-electric aircraft and beyond," *Proc. IEEE*, doi: 10.1109/JPROC.2022.3152995
- [4] S. Bozhko *et al.*, "Development of aircraft electric starter-generator system based on active rectification technology," *IEEE Trans. Transport. Electrification.*, vol. 4, no. 4, pp. 985-996, Dec. 2018.
- [5] Fang Zheng Peng, J. W. McKeever and D. J. Adams, "A power line conditioner using cascade multilevel inverters for distribution systems," *IEEE Trans. Ind. Appl.*, vol. 34, no. 6, pp. 1293-1298, Nov.-Dec. 1998.
- [6] M. F. Escalante, J.-C. Vannier and A. Arzande, "Flying capacitor multilevel inverters and DTC motor drive applications," *IEEE Trans. Ind. Electron.*, vol. 49, no. 4, pp. 809-815, Aug. 2002.
- [7] R. Sommer, A. Mertens, C. Brunotte, and G. Trauth, "Medium voltage drive system with NPC three-level inverter using IGBTs," in *Proc. IEEE Semin. PWM Medium Voltage Drives*, May 2000, pp. 3/1-3/5.
- [8] M. K. Mishra, A. Joshi, and A. Ghosh, "Control schemes for equalization of capacitor voltages in neutral clamped shunt compensator," *IEEE Trans. Power Del.*, vol. 18, no. 2, pp. 538-544, Apr. 2003.
- [9] J. Pou, D. Boroyevich and R. Pindado, "New feedforward space-vector PWM method to obtain balanced AC output voltages in a three-level neutral-point-clamped converter," *IEEE Trans. Ind. Electron.*, vol. 49, no. 5, pp. 1026-1034, Oct. 2002.
- [10] C. Wang and Y. Li, "Analysis and calculation of zero-sequence voltage considering neutral-point potential balancing in three-level NPC converters," *IEEE Trans. Ind. Electron.*, vol. 57, no. 7, pp. 2262-2271, Jul. 2010.
- [11] S. Busquets-Monge, J. Bordonau, D. Boroyevich and S. Somavilla, "The nearest three virtual space vector PWM - a modulation for the comprehensive neutral-point balancing in the three-level NPC inverter," *IEEE Power Electron. Lett.*, vol. 2, no. 1, pp. 11-15, Mar. 2004.
- [12] F. Guo, T. Yang, C. Li, S. Bozhko and P. Wheeler, "Active modulation strategy for capacitor voltage balancing of three-level neutral-point-clamped converters in high-speed drives," *IEEE Trans. Ind. Electron.*, vol. 69, no. 3, pp. 2276-2287, Mar. 2022.
- [13] Y. Yang *et al.*, "Low complexity finite-control-set MPC based on discrete space vector modulation for T-type three-phase three-level converters," *IEEE Trans. Power Electron.*, vol. 37, no. 1, pp. 392-403, Jan. 2022.
- [14] A. Choudhury, P. Pillay and S. S. Williamson, "DC-bus voltage balancing algorithm for three-level neutral-point-clamped (NPC) traction inverter drive with modified virtual space vector," *IEEE Trans. Ind. Appl.*, vol. 52, no. 5, pp. 3958-3967, Sep./Oct. 2016.
- [15] W. Jiang *et al.*, "A novel virtual space vector modulation with reduced common-mode voltage and eliminated neutral point voltage oscillation for neutral point clamped three-level inverter," *IEEE Trans. Ind. Electron.*, vol. 67, no. 2, pp. 884-894, Feb. 2020.
- [16] F. Guo, T. Yang, A. M. Diab, S. S. Yeoh, S. Bozhko and P. Wheeler, "An enhanced virtual space vector modulation scheme of three-level NPC converters for more-electric-aircraft applications," *IEEE Trans. Ind. Appl.*, vol. 57, no. 5, pp. 5239-5251, Sept.-Oct. 2021.
- [17] Department of Defense of United States of America, *Department of Defense Interface Standard—Aircraft Electric Power Characteristics*, Military Std. MIL-STD-704F, Mar. 2004.
- [18] F. Gao, S. Bozhko, A. Costabeber, G. Asher and P. Wheeler, "Control design and voltage stability analysis of a droop-controlled electrical power system for more electric aircraft," *IEEE Trans. Ind. Electron.*, vol. 64, no. 12, pp. 9271-9281, Dec. 2017.
- [19] J. Ebersberger, M. Hagedorn, M. Lorenz and A. Mertens, "Potentials and comparison of inverter topologies for future all-electric aircraft propulsion," *IEEE J. Emerg. Sel. Topics Power Electron.*, vol. 10, no. 5, pp. 5264-5279, Oct. 2022.
- [20] S. Bifaretti, A. Lidozzi, L. Solero and F. Crescimbin, "Modulation with sinusoidal third-harmonic injection for active split dc-bus four-leg inverters," *IEEE Trans. Power Electron.*, vol. 31, no. 9, pp. 6226-6236, Sept. 2016.
- [21] H. Wang *et al.*, "Two-stage matrix converter based on third-harmonic injection technique," *IEEE Trans. Power Electron.*, vol. 31, no. 1, pp. 533-547, Jan. 2016.
- [22] M. J. Duran, F. Salas and M. R. Arahal, "Bifurcation analysis of five-phase induction motor drives with third harmonic injection," *IEEE Trans. Ind. Electron.*, vol. 55, no. 5, pp. 2006-2014, May 2008.
- [23] G. Guo *et al.*, "Application of third-order harmonic voltage injection in a modular multilevel converter," *IEEE Trans. Ind. Electron.*, vol. 65, no. 7, pp. 5260-5271, July 2018.

- [24] J. Holtz, W. Lotzkat and A. M. Khambadkone, "On continuous control of PWM inverters in the overmodulation range including the six-step mode," *IEEE Trans. Power Electron.*, vol. 8, no. 4, pp. 546-553, Oct. 1993.
- [25] Dong-Choon Lee and G-Myoung Lee, "A novel overmodulation technique for space-vector PWM inverters," *IEEE Trans. Power Electron.*, vol. 13, no. 6, pp. 1144-1151, Nov. 1998.
- [26] K. Sun, Q. Wei, L. Huang and K. Matsuse, "An overmodulation method for PWM-inverter-fed IPMSM drive with single current sensor," *IEEE Trans. Ind. Electron.*, vol. 57, no. 10, pp. 3395-3404, Oct. 2010.
- [27] P. Stumpf and S. Halász, "Optimization of PWM for the overmodulation region of two-level inverters," *IEEE Trans. Ind. Appl.*, vol. 54, no. 4, pp. 3393-3404, Jul./Aug. 2018.
- [28] S. K. Giri, S. Mukherjee, S. Kundu, S. Banerjee and C. Chakraborty, "An improved PWM scheme for three-level inverter extending operation into overmodulation region with neutral-point voltage balancing for full power-factor range," *IEEE J. Emerg. Sel. Topics Power Electron.*, vol. 6, no. 3, pp. 1527-1539, Sep. 2018.
- [29] S. Busquets-Monge, R. Maheshwari and S. Munk-Nielsen, "Overmodulation of  $n$ -level three-leg DC-AC diode-clamped converters with comprehensive capacitor voltage balance," *IEEE Trans. Ind. Electron.*, vol. 60, no. 5, pp. 1872-1883, May 2013.
- [30] F. Guo *et al.*, "An overmodulation algorithm with neutral-point voltage balancing for three-level converters in high-speed aerospace drives," *IEEE Trans. Power Electron.* vol. 37, no. 2, pp. 2021-2032, Feb. 2022.
- [31] F. Guo, T. Yang, S. S. Yeoh, S. Bozhko, P. Wheeler and A. M. Diab, "A simple PWM strategy for three-level NPC converters in aircraft electric starter/generator system with improved DC-link voltage utilization and reduced common-mode voltage," in *Proc. IEEE Energy Convers. Congr. Expo.*, Vancouver, BC, Canada, 2021, pp. 4854-4858.
- [32] A. Choudhury, P. Pillay and S. S. Williamson, "Modified DC-bus voltage balancing algorithm for a three-level neutral-point-clamped PMSM inverter drive with reduced common-mode voltage," *IEEE Trans. Ind. Appl.*, vol. 52, no. 1, pp. 278-292, Jan.-Feb. 2016.
- [33] A. Choudhury and P. Pillay, "Space vector based capacitor voltage balancing for a three-level NPC traction inverter drive," *IEEE J. Emerg. Sel. Topics Power Electron.*, vol. 8, no. 2, pp. 1276-1286, Jun. 2020.
- [34] C. Li *et al.*, "A modified neutral point balancing space vector modulation for three-level neutral point clamped converters in high-speed drives," *IEEE Trans. Ind. Electron.*, vol. 66, no. 2, pp. 910-921, Feb. 2019.
- [35] S. Mukherjee, S. K. Giri and S. Banerjee, "A flexible discontinuous modulation scheme with hybrid capacitor voltage balancing strategy for three-level NPC traction inverter," *IEEE Trans. Ind. Electron.*, vol. 66, no. 5, pp. 3333-3343, May 2019.
- [36] G. Nadh and A. Rahul S, "Clamping modulation scheme for low-speed operation of three-level inverter fed induction motor drive with reduced CMV," *IEEE Trans. Ind. Appl.*, vol. 58, no. 6, pp. 7336-7345, Nov.-Dec. 2022.
- [37] B. Chikondra, U. R. Muduli and R. K. Behera, "Improved DTC technique for THL-NPC VSI fed five-phase induction motor drive based on VVs assessment over a wide speed range," *IEEE Trans. Power Electron.*, vol. 37, no. 2, pp. 1972-1981, Feb. 2022.



**Feng Guo** (Member) received his B.Eng. from China University of Mining and Technology, Xuzhou, China, in 2014, and received M.S. (Hons.) from Northeastern University, Shenyang, China, in 2017, both in electrical engineering, and the Ph.D. degree at the Power Electronics, Machines and Control (PEMC) Research Group in electrical and electronics engineering from the University of Nottingham, Nottingham, U.K., in 2021.

Since January 2022, he has been with the Power Electronic Systems Laboratory at Arkansas (PESLA), University of Arkansas, Fayetteville, AR, USA, as a Postdoctoral Research Fellow. From 2016 to 2017, he was a visiting student at the Chinese University of Hong Kong, Shenzhen, China. His research interests include pulse-width-modulation strategy, high efficiency and high power-density multilevel converters, wide bandgap power device applications, high-speed motor drives, fast charging technologies and transportation

electrification, etc. He was the recipient of the 2017 Outstanding Graduate Student Award and the 2022 IEEE Industry Applications Society (IAS) Transactions Second Place Prize Paper Award.



**Ahmed M. Diab** (Student Member) received the B.Sc. (Hons.) and M.Sc. degrees in electrical power and machine engineering from Zagazig University, Zagazig, Egypt in 2011 and 2016, respectively. He is currently working toward a Ph.D. degree at the University of Nottingham Ningbo China and the Institute for Aerospace technology (IAT), University of Nottingham, Nottingham, UK. From 2011 to 2016, he was a research

and Teaching Assistant with the Department of Electrical Power and Machines, at Zagazig University. His research interests include modeling, control, and stability in high-speed motor/generator systems for transportation electrification applications and in variable-speed wind generators.



**Seang Shen Yeoh** received his MSc degree in power electronics (Distinction) and Ph.D. degree in electrical engineering from the University of Nottingham, United Kingdom, in 2011 and 2016 respectively. Since then, he has been a senior research fellow at the same university under the Power Electronics, Machines, and Controls Research Group. His current research interests are in the area of aircraft power systems, namely modeling and stability

studies of complex power systems, and new control strategies for high-speed drive systems.



**Tao Yang** (Senior Member) received his MEng Degree from Shanghai Jiao Tong University, China in 2008 and his Ph.D. degree in electrical engineering from the University of Nottingham, UK in 2013.

Since 2013, he has been a Researcher with Power Electronics, Machines and Control Group, University of Nottingham, where he became an Assistant Professor in 2016, and an Associate Professor in 2019. His research interests include high-speed electric motor drive control, power electronic conversion, electrical system design and optimization for more electric/hybrid/all-electric aircraft applications. His PhD research within EU Clean Sky on "Modelling electrical power system for more-electric aircraft applications" has resulted in him winning the inaugural "Clean Sky Best PhD Award" in 2016. Dr. Yang is an Associate Editor for the IEEE TRANSACTIONS ON TRANSPORTATION ELECTRIFICATION and Chinese Journal of Aeronautics.



**Serhiy Bozhko** (Senior Member) received his M.Sc. and Ph.D. degrees in electromechanical systems from the National Technical University of Ukraine, Kyiv City, Ukraine, in 1987 and 1994, respectively. Since 2000, he has been with the Power Electronics, Machines and Controls Research Group of the University of Nottingham, United Kingdom, where currently he is Professor of Aircraft Electric Power Systems and Director of the

Institute for Aerospace Technology. He is leading several EU- and

industry-funded projects in the area of aircraft electric power systems, including power generation, distribution and conversion, power quality, control and stability issues, power management and optimization, as well as advanced modelling and simulations methods.



**Patrick Wheeler** (Fellow) received his BEng [Hons] degree in 1990 from the University of Bristol, UK. He received his PhD degree in Electrical Engineering for his work on Matrix Converters from the University of Bristol, UK in 1994. In 1993 he moved to the University of Nottingham and worked as a research assistant in the Department of Electrical and Electronic Engineering. In 1996 he became a Lecturer

in the Power Electronics, Machines and Control Group at the University of Nottingham, UK. Since January 2008 he has been a Full Professor in the same research group.

He is currently the Global Engagement Director For the Faculty of Engineering, the Head of the Power Electronics, Machines and Control Research Group and the Director of the University of Nottingham's Institute of Aerospace Technology He was Head of the Department of Electrical and Electronic Engineering at the University of Nottingham from 2015 to 2018. He is a member of the IEEE PELs AdCom and is currently IEEE PELs Vice-President for Technical Operations. He has published over 850 academic publications in leading international conferences and journals.



**Yue Zhao** (Senior Member) received a B.S. degree in electrical engineering from Beijing University of Aeronautics and Astronautics, Beijing, China, in 2010, and a Ph.D. degree in electrical engineering from the University of Nebraska-Lincoln, Lincoln, USA, in 2014.

He was an Assistant Professor in the Department of Electrical and Computer Engineering at the Virginia Commonwealth University, Richmond, USA, in 2014-2015. Since August 2015, he has been with the University of Arkansas (UA), Fayetteville, USA, where he is currently an Associate Professor in the Department of Electrical Engineering. He also serves as the Executive Director for the National Science Foundation (NSF) I/UCRC on GRid-connected Advanced Power Electronic Systems (GRAPES). His current research interests include electric machines and drives, power electronics, and renewable energy systems. He has 4 U.S. patents granted and co-authored more than 130 papers in refereed journals and international conference proceedings.

Dr. Zhao is an Associated Editor of the IEEE Transactions on Industry Applications and IEEE Open Journal of Power Electronics. He was a recipient of 2018 NSF CAREER Award, the 2020 IEEE Industry Applications Society Andrew W. Smith Outstanding Young Member Achievement Award and the 2020 UA College of Engineering Dean's Award of Excellence.